HHS Public Access

Author manuscript

Annu Int Conf IEEE Eng Med Biol Soc. Author manuscript; available in PMC 2021 July 01.

Published in final edited form as:

Annu Int Conf IEEE Eng Med Biol Soc. 2020 July ; 2020: 2023–2026. doi:10.1109/EMBC44109.2020.9175319.

Adaptation of Dictionary Learning for Electrode Displacement Elastography

Robert M. Pohlman [Member, IEEE],

Department of Electrical Engineering and Medical Physics, University of Wisconsin School of Medicine and Public Health (UW-SMPH), University of Wisconsin-Madison, Madison, WI 53706, USA

Tomy Varghese [Senior Member, IEEE]

Department of Medical Physics, UW-SMPH, Department of Electrical Engineering and Biomedical Engineering, University of Wisconsin-Madison, Madison, WI 53706, USA

Abstract

Microwave ablation has become a common treatment method for liver cancers. Unfortunately, microwave ablation success is correlated with clinician's ability for proper electrode placement and assess ablative margins, requiring accurate imaging of liver tumors and ablated zones. Conventionally, ultrasound and computed tomography are utilized for this purpose, yet both have their respective drawbacks. As an alternate approach, electrode displacement elastography offers promise but is still plagued by decorrelation artifacts reducing lesion depiction and visualization. A recent filtering method, namely dictionary representation, has improved contrast-to-noise ratios without reducing delineation contrast. As a supplement to this recent work, this paper evaluates adaptations on this initial dictionary-learning algorithm and applies them to an EDE phantom and 15 in-vivo patient datasets. Two new adaptations of dictionary representations were evaluated, namely a combined dictionary and magnitude-based dictionary representation. When comparing numerical results, the combined dictionary representation algorithm outperforms the previous developed dictionary representation in signal-to-noise (1.54 dB) and contrast-to-noise (0.67 dB) ratios, while a magnitude dictionary representation produces higher noise levels, but improves visualized strain tensor resolution.

I. Introduction

Surgical techniques such as resection and transplantation are the gold-standard for treatment of liver cancers [1]. Unfortunately 3 out of 4 patients are not viable candidates due to multiple or advanced metastatic disease, recurrent tumors, low hepatic reserve, and medical comorbidities [2]. Minimally invasive procedures are therefore being offered to patients with survival results similar to surgical resection [3]. Utilization of minimally invasive procedures, such as microwave ablation (MWA), are favorable as it reduces surgical morbidity, mortality, and large incisions to patients [4]. These treatments are also of lower cost and allow for repeated treatments if needed to improve survival [5]. However to achieve

(phone: 815-298-6491; rpohlman2@wisc.edu).

proper treatment using MWA, correct energy delivery, proper electrode placement, and most importantly verification of minimal ablative margins are needed, all of which require accurate image representation of pre and post ablation regions [6].

Commonly, MWA suites utilize ultrasound and computed tomography (CT) during procedures for visualizing pre-ablation tumors and assessing post-ablation regions. Here, CT's role validates microwave electrode placement and post-ablation margins, however Contrast Enhanced CT (CECT) is time-consuming, costly, and results in radiation exposure. On the other hand, ultrasound is nonionizing and provides real-time guidance of electrode placement and approximate monitoring of ablation progress [7]. Ultrasound alone may not produce sufficient contrast and can overestimate the size of ablated areas [8].

An alternative to ultrasound and CT, less commonly used in clinical procedures is elastography, specifically electrode displacement elastography (EDE) [9]. EDE uses quasi-static deformations induced by electrode perturbations to visualize local stiffness differences in tissue with high contrast-to-noise ratios (CNR). EDE has been validated in phantoms, animal models, and *in vivo* patient data [10–12].

Unfortunately, displacement estimation in EDE is a noisy process making visualizing liver tumors at deeper depths and low signal-to-noise ratios (SNR) difficult [13]. A Multilevel 2D Normalized Cross-Correlation (MNCC) algorithm was used due to its high success rates and CNR for EDE [12]. Methods to combat decorrelation noise such as companding, regularization, and temporal stretching have been implemented, yet noise artifacts are still a problem [14–16]. We recently utilized dictionary learning to denoise displacement estimates which maintained contrast while reducing noise [17]. The goal in this paper was to improve the dictionary learning process for phantom and *in-vivo* datasets. Novel variations of dictionary-learning algorithms were also evaluated.

II. Methods

The protocol used for analysis in this paper is shown in Fig. 1, where the red box labeled filtering incorporates adapted dictionary learning [17]. Flowchart steps in Fig. 1 are further described in the following sections.

A. Data Collection and Displacement Estimation

Radiofrequency (RF) data was collected using a Siemens S2000 (Siemens Inc., CA, USA) system with a 6C1 HD curvilinear transducer on an EDE phantom with deformations introduced using an actuator [17]. Fifteen independent datasets were collected using the ultrasound research interface (URI) on the system [17].

In-vivo RF data on patients was collected during MWA procedures at the University of Wisconsin (UW)-Madison Hospitals and clinics following a protocol approved by the health sciences institutional review board at UW-Madison. All 15 patients involved in this study provided informed consent prior to the procedure. During the procedure, 80 RF frames were acquired after ablation during which clinicians perturbed the electrode by approximately 1 mm. Signal and image processing was performed offline in MATLAB to obtain

displacement vectors and strain tensors. Displacement estimates were obtained using the MNCC method described in [18] using the procedure in [17].

B. Filtering Displacement Estimates

Each displacement filtering method is shown in Table 1. Median filtering utilized a kernel size of 1.9 × 1.9 mm and dictionary representation [17] utilized a patch size of 4.0 × 4.0 mm and 80% patch overlap with dictionaries learned directly from displacement estimates to be filtered. To maintain consistency, a single displacement frame showing largest cross-sectional area was manually selected for each patient by an untrained observer for comparison.

When filtering using the individual dictionary method, the initial dictionary is selected as image patches with the highest energy directly from the image to be denoised. An iterative dictionary learning algorithm alternates between updating the dictionary and coefficients using block-coordinate descent. Finally the algorithm is repeated individually for axial and lateral displacement vectors [17]. Conversely, for a combined representation, the dictionary learning process had to be linked, where coefficients and denoised displacement image for axial and lateral vectors were obtained using the combined dictionary representation in (1), where X denotes denoised displacement estimates, Y the median filtered noisy displacement estimates, subscripts Ax and Lat refer to axial and lateral displacement vectors respectively, and R_{ij} is the matrix which extracts the (i, j) block from the displacement map. After each iteration of minimizing (1), the coefficient vector, α_{Comb}, was updated using (2) from the new updated α_{Ax} and α_{Lat}. Here $\phi = 0.5$ was used to dictate the weight of the axial and lateral coefficient vector onto the combined coefficient vector, where $\phi = 0$ used only axial updated coefficient vector and $\phi = 1$ used only lateral. Similar to learning the individual dictionary, the axial and lateral combined dictionaries, D_{Ax} and D_{Lat}, were found using a common coefficient vector as shown in (3).

$$\begin{aligned}\{\alpha_{Ax}, X_{Ax}\} &= \arg\min_{\alpha_{Ax}, X_{Ax}} \lambda\|X_{Ax} - Y_{Ax}\|_2^2 \\ &\quad + \sum_{ij} \mu_{sparse}\|\alpha_{Comb}\|_1 + \sum_{ij} \|D_{Ax}\alpha_{Comb} - R_{ij}Y_{Ax}\|_2^2 \\ \{\alpha_{Lat}, X_{Lat}\} &= \arg\min_{\alpha_{Lat}, X_{Lat}} \lambda\|X_{Lat} - Y_{Lat}\|_2^2 \\ &\quad + \sum_{ij} \mu_{sparse}\|\alpha_{Comb}\|_1 + \sum_{ij} \|D_{Lat}\alpha_{Comb} - R_{ij}Y_{Lat}\|_2^2\end{aligned} \tag{1}$$

$$\alpha_{Comb} = \phi(\alpha_{Lat} - \alpha_{Ax}) + \alpha_{Ax} \tag{2}$$

$$\min_{\|\alpha\|_0 \le \kappa} [\|y_{Axial} - D_{Axial}\alpha\| + \|y_{Lateral} - D_{Lateral}\alpha\|] \tag{3}$$

The magnitude of the dictionary representation was also utilized. Displacement estimates contain both axial (dy) and lateral (dx) components represented as a magnitude vector ($\vec{d}$) and phase angle (θ) shown in Fig. 2. This allows a single individual dictionary to be learned

by using $\vec{d}$ as displacements in the individual dictionary representation algorithm. Strain tensors can be directly estimated from the magnitude displacement map or decomposed into axial and lateral components before strain tensor calculation. All strain tensors were estimated using a 2D Savitzky-Golay digital differentiator of size 0.2 × 5.0 mm using 0^{th} × 2^{nd} order polynomials for x and y directions respectively [19].

III. Results

After displacement estimation using MNCC, all filtering methods described in Table 1 were done, followed by strain tensor calculation. First, quantitative metrics were obtained for each filtering method. Target and background ROIs were placed to calculate SNR, contrast, and CNR for all methods as defined in [12].

EDE phantom metrics are shown in Table 2. The combined dictionary provides highest SNR and CNR, with a slight reduction in contrast. Magnitude dictionaries have higher SNR, contrast, and CNR than the original and median filtered results, but lower than other dictionary methods.

In-vivo strain tensor metrics are shown by boxplots in Fig. 3, where (a) shows SNR, (b) contrast, and (c) CNR with axial results in blue and lateral results in red. SNR distributions in Fig. 3 (a) show very little difference between original and median filtering approaches. For dictionary representations, individual and combined dictionaries show very similar results, where axial SNR shows the highest values with the combined dictionary representation. Axial SNR shows the tightest and highest distribution with mean and standard deviation of 4.38 ± 0.69 dB. Magnitude vector dictionary provides the lowest values with mean of 1.31 dB, while magnitude components provide higher median values of means 2.39 dB and 2.86 dB for axial and lateral respectively. Magnitude also has the widest distribution with standard deviations of 1.4 dB axially and 1.98 dB laterally indicating inconsistent SNR across patients.

Contrast distributions shown in Fig. 3 (b) have similar results for original with means of 26.0 dB and 15.0 dB and median filtering with means of 26.6 dB and 15.6 dB. On the other hand, lateral individual, lateral combined, and magnitude vector dictionaries show similar distributions with mean values of 21.7, 20.6, and 20.8 dB respectively. Axial individual and combined dictionaries show similar tight distribution widths with standard deviations of 2.2 and 1.5 dB. Individual dictionary representations have the highest and tightest contrast distribution with mean of 26.7 dB. CNR distributions are shown in Fig. 3 (c), where again original and median filtered distributions look very similar with mean and standard deviations of 1.92 ± 1.09 dB and 2.15 ± 1.02 dB axially and 2.34 ± 0.70 dB and 2.60 ± 0.64 dB laterally. However, CNR distributions of individual and combined dictionaries are much higher than other distributions with combined dictionary having the highest in axial and lateral directions with means of 3.90 ± 0.45 dB and 4.08 ± 0.84 dB. Magnitude vector distribution was the lowest of all methods with mean of 1.86 ± 0.63 dB.

Overall, the combined dictionary learning algorithm improved SNR and CNR by 1.54 dB (26%) and 0.67 dB (12%) when compared to the individual dictionary learning, while also

showing a decrease in contrast by 2.18 dB (13%) for EDE phantom data. Similarly, the combined dictionary improved SNR and CNR by approximately 0.17 dB (4.0%) and 0.63 dB (19%), while also showing a decrease in contrast by 2.2 dB (8.2%) for *in-vivo* patients.

Finally, visualization using each of the filtering methods from Table 1 are shown for an EDE phantom in Fig. 4 and a patient with colon cancer metastasized to the liver in Fig. 5. The approximate location of the ablation zone shown in Fig. 4 (a) were matched both by size and location in strain tensor images in Fig. 4 (b–h). Observe in Figs. 4 (c, e) the gradual increase in lesion boundary contrast and lowered noise within the ablated region as well as lower noise outside. Lateral images in Figs. 4 (d, f) depict a smaller ablated zone, with reduced boundary smoothness. However, noise reduction in lateral strain tensor images is similar to that seen with axial strain, with the lowest noise and best boundary delineation obtained with the combined dictionary. However, with magnitude component images in Fig. 4 (g) and (h), an increase in pixel resolution is seen with a increase in the noise level. Similarly, the magnitude image in Fig. 4 (b) shows lower boundary smoothness and high noise levels. Despite varying levels of contrast and noise, all filtering methods maintain lesion visualization in a similar location as seen on the B-mode image, i.e. Fig. 4 (a). Similar to phantom results, the *in-vivo* strain tensor images in Fig. 5 show the lowest noise and highest boundary contrast from the combined dictionary representation, while the magnitude component dictionary representations show increased pixel resolution but also higher noise levels.

IV. Conclusion

We compare metrics using an EDE phantom and 15 *in vivo* patient strain tensor images using dictionary learning and adaptations to original and median filtered displacement estimates. EDE phantom data shows that combined axial and lateral dictionary-learning algorithms had the highest SNR and CNR with improvements of 3.90 dB and 6.58 dB for axial strain tensors compared to unfiltered images. In contrast, magnitude dictionaries did not reduce strain tensor noise and decreased SNR, contrast, and CNR compared to original displacement estimates. Future work will extend these new dictionary algorithms for use in Lagrangian tracking [20] and comparison with the clinical gold-standard, CECT, for assessing post-ablation volumes [21].

Acknowledgment

We are grateful to Siemens Medical Solutions USA, Inc., for providing the S2000 Axius Direct URI and software licenses.

Research supported by NIH grant 2R01 CA112192, 1R01 HL147866-01 and T32 CA009206.

References

[1]. Liu L-X, Zhang W-H, and Jiang H-C, “Current treatment for liver metastases from colorectal cancer,” World J Gastroentero, vol. 9, p. 193, 2003.

[2]. Bipat S, van Leeuwen MS, Ijzermans J, Comans E, Planting A, Bossuyt P, et al., “Evidence-base guideline on management of colorectal liver metastases in the Netherlands,” Neth. J. Med, vol. 65, pp. 5–14, 2007. [PubMed: 17293634]

[3]. Poulou LS, Botsa E, Thanou I, Ziakas PD, and Thanos L, “Percutaneous microwave ablation vs radiofrequency ablation in the treatment of hepatocellular carcinoma,” World J. of Hepatol, vol. 7, p. 1054, 2015. [PubMed: 26052394]

[4]. Tang XY, Wang Z, Wang T, Cui D, and Zhai B, “Efficacy, safety and feasibility of ultrasound-guided percutaneous microwave ablation for large hepatic hemangioma,” J Dig. Dis, vol. 16, pp. 525–530, 2015. [PubMed: 24945806]

[5]. Martin RC, Scoggins CR, and McMasters KM, “Safety and efficacy of microwave ablation of hepatic tumors: a prospective review of a 5-year experience,” Ann. Surg. Oncol, vol. 17, pp. 171–178, 2010. [PubMed: 19707829]

[6]. Meloni MF, Chiang J, Laeseke PF, Dietrich CF, Sannino A, Solbiati M, et al., “Microwave ablation in primary and secondary liver tumours: technical and clinical approaches,” Int. J. Hyperther, vol. 33, pp. 15–24, 2017.

[7]. Lee MW, Kim YJ, Park HS, Yu NC, Jung SI, Ko SY, et al., “Targeted sonography for small hepatocellular carcinoma discovered by CT or MRI: factors affecting sonographic detection,” Am. J. Roentgenol, vol. 194, pp. W396–W400, 2010. [PubMed: 20410384]

[8]. Hoffmann R, Rempp H, Keßler D-E, Weiß J, Pereira PL, Nikolaou K, et al., “MR-guided microwave ablation in hepatic tumours: initial results in clinical routine,” Eur. Rad, vol. 27, pp. 1467–1476, 2017.

[9]. Varghese T, Zagzebski JA, and Lee FT, “Elastographic imaging of thermal lesions in the liver in vivo following radiofrequency ablation: preliminary results,” Ultrason. Med. Biol, vol. 28, pp. 1467–1473, 2002/11 2002.

[10]. Bharat S, Varghese T, Madsen EL, and Zagzebski JA, “Radio-frequency ablation electrode displacement elastography: a phantom study,” Med. Phys, vol. 35, pp. 2432–42, 6 2008. [PubMed: 18649476]

[11]. Rubert N, Bharat S, DeWall RJ, Andreano A, Brace C, Jiang J, et al., “Electrode displacement strain imaging of thermally-ablated liver tissue in an in vivo animal model,” Med. Phys, vol. 37, pp. 1075–1082, 2010. [PubMed: 20384243]

[12]. Pohlman RM, Varghese T, Jiang J, Ziemlewicz TJ, Alexander ML, Wergin KL, et al., “Comparison of Displacement Tracking Algorithms for in Vivo Electrode Displacement Elastography,” Ultrason. Med. Biol, vol. 45, pp. 218–232, 2019.

[13]. Cespedes I and Ophir J, “Reduction of image noise in elastography,” Ultrason. Imag, vol. 15, pp. 89–102, 1993.

[14]. Meshram NH and Varghese T, “GPU accelerated multilevel Lagrangian Carotid Strain Imaging,” IEEE Trans. Ultrason. Ferroel. Freq. Cont, vol. 65, pp. 1370–1379, August 2018 2018.

[15]. McCormick M, Rubert N, and Varghese T, “Bayesian Regularization Applied to Ultrasound Strain Imaging,” IEEE Trans. on Biomed. Eng, vol. 58, pp. 1612–1620, 2011.

[16]. Brusseau E, Kybic J, Deprez JF, and Basset O, “2-D locally regularized tissue strain estimation from radio-frequency ultrasound images: theoretical developments and results on experimental data,” IEEE Trans. Med. Imag, vol. 27, pp. 145–60, 2 2008.

[17]. Pohlman RM and Varghese T, “Dictionary Representations for Electrode Displacement Elastography,” IEEE IEEE Trans. Ultrason. Ferroel. Freq. Cont, vol. 65, pp. 2381–2389, 2018.

[18]. Shi H and Varghese T, “Two-dimensional multi-level strain estimation for discontinuous tissue,” Phys. Med. Biol, vol. 52, pp. 389–401, 1 21 2007. [PubMed: 17202622]

[19]. Luo J, Ying K, He P, and Bai J, “Properties of Savitzky–Golay digital differentiators,” Dig. Sig. Proc, vol. 15, pp. 122–136, 2005.

[20]. Pohlman RM and Varghese T, “Physiological Motion Reduction Using Lagrangian Tracking for Electrode Displacement Elastography,” Ultrason. Med. Biol, 2019, 10.1016/j.ultrasmedbio.2019.11.001.

[21]. Pohlman RM, Turney MR, Wu PH, Brace CL, Ziemlewicz TJ, and Varghese T, “Two-dimensional ultrasound-computed tomography image registration for monitoring percutaneous hepatic intervention,” Med. Phys, vol. 46, no. 6, pp. 2600–2609, 2019, 10.1002/mp.13554. [PubMed: 31009079]

Clinical Relevance—

Dictionary learning provides improved visualization of post microwave ablation with electrode displacement elastography

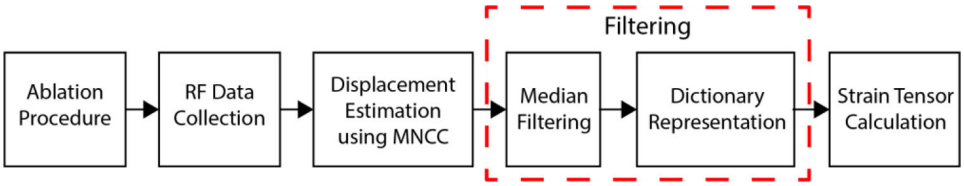

Figure 1 –.

The flowchart from ablation procedure to producing strain tensor images for electrode displacement elastography. Red box of filtering is the portion of flowchart that was varied based on Table 1.

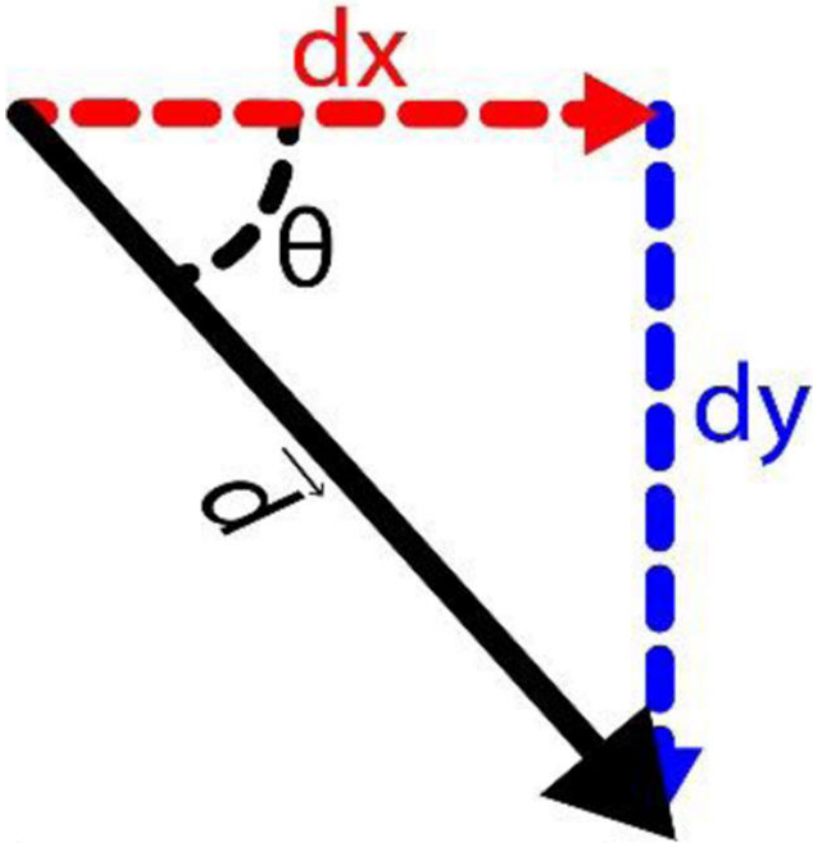

Figure 2 –.

Displacement estimation variations of axial (dy) and lateral (dx) or magnitude ($\vec{d}$) and phase (θ).

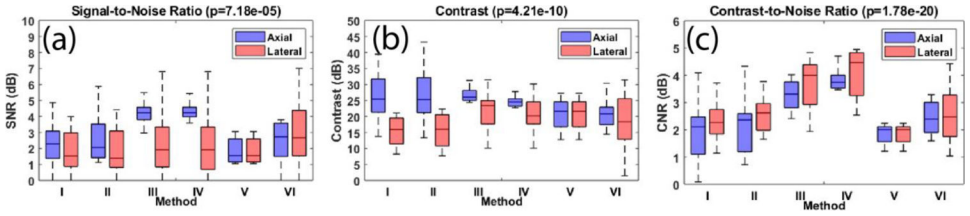

Figure 3 –.

Distributions (n=15) of signal-to-ratio (a), contrast (b), and contrast-to-noise ratio (c) for all filtering variations used where I is unfiltered, II is median filtered, III is individual dictionary, IV is combined dictionary, V is magnitude dictionary vector, and VI is magnitude dictionary.

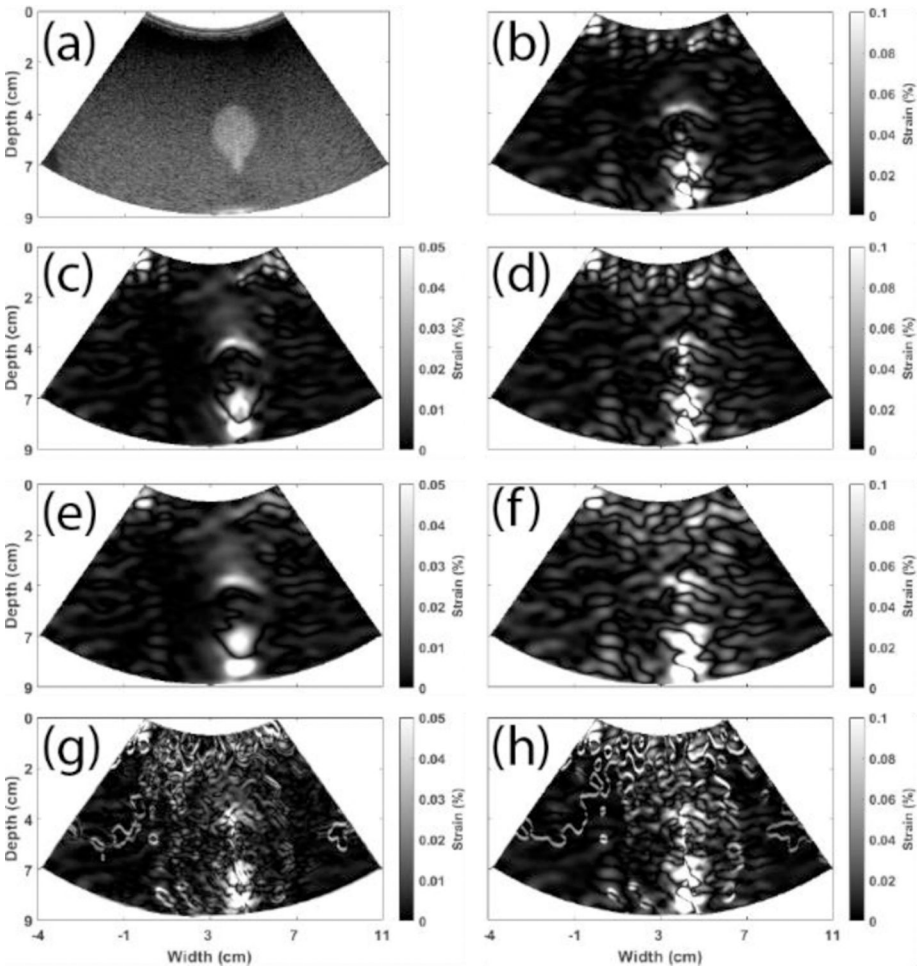

Figure 4 –.

B-mode and strain tensor images from an EDE phantom. Ablation antenna artifact is seen near distal boundary of the inclusion. (a) B-mode, and strain tensor images from (b) magnitude vector dictionary, (c) individual dictionary axial, (d) individual dictionary lateral, (e) combined dictionary axial, (f) combined dictionary lateral, (g) magnitude dictionary axial, and (h) magnitude dictionary lateral component.

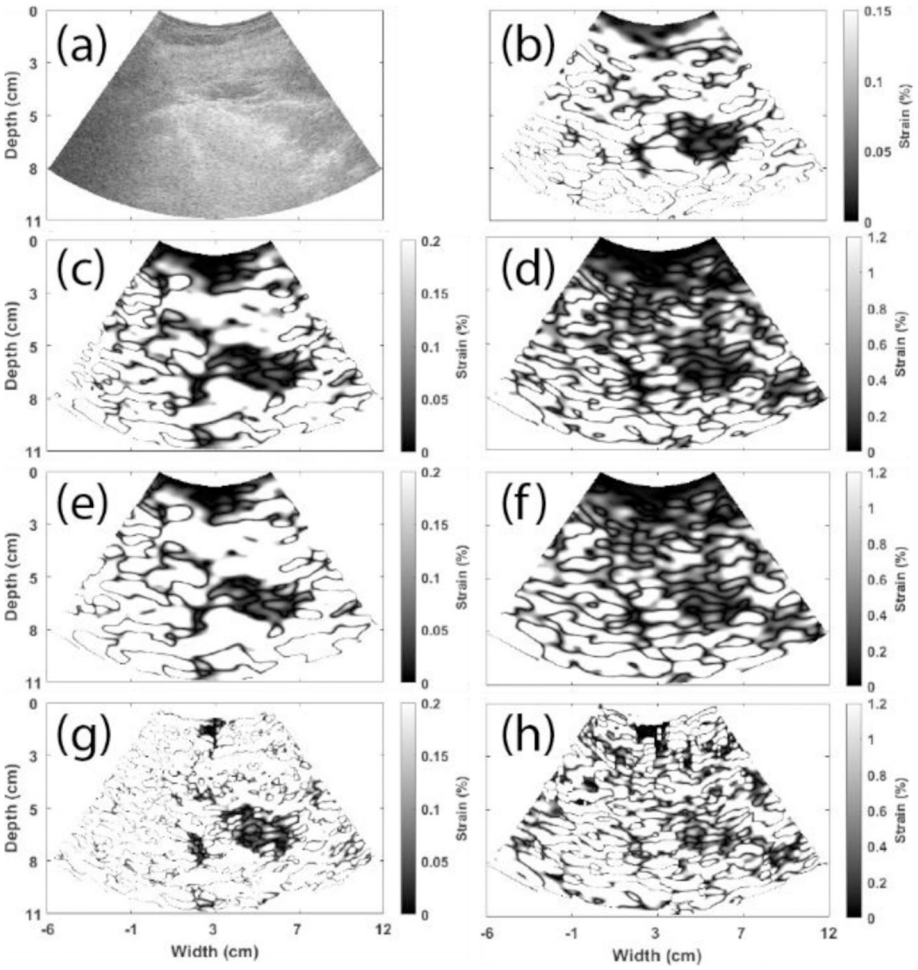

Figure 5 –.

Ultrasound B-mode and strain tensor images from a post-MWA patient with colon cancer metastasized to the liver. (a) B-mode, and strain tensor images from (b) magnitude vector dictionary, (c) individual dictionary axial, (d) individual dictionary lateral, (e) combined dictionary axial, (f) combined dictionary lateral, (g) magnitude dictionary axial and (h) magnitude dictionary lateral component.

Table 1 –

Description of various filtering methods utilized in this work.

	FILTERING METHOD	DESCRIPTION OF FILTERING METHOD
I	**UNFILTERED**	No filtering of displacement estimates from MNCC algorithm.
II	**MEDIAN FILTERING**	Median filtering only.
III	**INDIVIDUAL DICTIONARY**	After median filtering, dictionary representation of dx and dy separately.
IV	**COMBINED DICTIONARY**	After median filtering, dictionary representation linking patches of dx and dy together using Eq. (1).
V	**MAGNITUDE VECTOR DICTIONARY**	After median filtering, dictionary representation of $\overrightarrow{d}$.
VI	**MAGNITUDE COMPONENT DICTIONARY**	After median filtering, dictionary representation of $\overrightarrow{d}$ then converting displacements back to dx and dy vectors.

Table 2 –

Mean (μ) and standard deviation (σ) of various filtering methods on 15 axial strain tensor images from EDE phantom data.

	SNR			CONTRAST			CNR		
METHOD	**μ**		**σ**	**μ**		**σ**	**μ**		**σ**
I	3.57	±	2.18	8.14	±	7.40	−0.48	±	5.18
II	3.27	±	3.11	8.83	±	7.77	0.74	±	2.82
III	5.93	±	5.47	17.44	±	2.79	5.43	±	1.09
IV	7.47	±	6.14	15.26	±	3.70	6.10	±	1.57
V	5.01	±	2.18	13.85	±	5.57	3.84	±	2.66
VI	4.25	±	0.88	9.43	±	8.12	0.17	±	3.01